Three-Dimensional Elastic-Plastic Stress Analysis of Rolling Contact

Yanyao Jiang
e-mail: yjiang@unr.edu
Assoc. Prof.,
Mem. ASME

Biqiang Xu
Research Fellow

University of Nevada,
Department of Mechanical Engineering (312),
Reno, NV 89557

Huseyin Sehitoglu
Grayce Wicall Gauthier Professor
University of Illionois,
Department of Mechanical Engineering,
Urbana, IL 61801

Three-dimensional elastic-plastic rolling contact stress analysis was conducted incorporating elastic and plastic shakedown concepts. The Hertzian distribution was assumed for the normal surface contact load over a circular contact area. The tangential forces in both the rolling and lateral directions were considered and were assumed to be proportional to the Hertzian pressure. The elastic and plastic shakedown limits obtained for the three-dimensional contact problem revealed the role of both longitudinal and lateral shear traction on the shakedown results. An advanced cyclic plasticity model was implemented into a finite element code via the material subroutine. Finite element simulations were conducted to study the influences of the tangential surface forces in the two shear directions on residual stresses and residual strains. For all the cases simulated, the p_0/k ratio (p_0 is the maximum Hertzian pressure and k is the yield stress in shear) was 6.0. The Q_x/P ratio, where Q_x is the total tangential force on the contact surface in the rolling direction and P is the total normal surface pressure, ranged from 0 to 0.6. The Q_y/P ratio (Q_y is the total tangential force in the lateral direction) was either zero or 0.25. Residual stresses increase with increasing rolling passes but tend to stabilize. Residual strains also increase but the increase in residual strain per rolling pass (ratchetting rate) decays with rolling cycles. Residual stress levels can be as high as 2k when the Q_x/P ratio is 0.6. Local accumulated shear strains can exceed 20 times the yield strain in shear after six rolling passes under extreme conditions. Comparisons of the two-dimensional and three-dimensional rolling contact results were provided to elucidate the differences in residual stresses and ratchetting strain predictions. [DOI: 10.1115/1.1491978]

1 Introduction

Rolling contact refers to the relative angular motion between two bodies in contact about an axis parallel to their common tangent plane [1]. It can be found in many engineering applications. The action between a wheel and a rail is a typical example. There is an increased interest in railroad industry in the use of high adhesion locomotives. The achievement of high adhesion levels through control of wheel creep can generate higher traction forces and heavier load in service. Currently, the locomotive wheel/rail adhesion levels are nearing 50 percent under conditions of finite percentage of creep. A major failure mode under these conditions is fatigue that results from cyclic stresses and strains. Excessive accumulation of plastic strains in rolling contact also contributes to the failure of a rolling element.

To better assess rolling contact failure, it is critical to understand the rolling contact stresses and strains. Elastic solutions for rolling contact are available in analytical forms [2–4]. However, most rolling contact actions result in cyclic plastic deformation. Two types of approaches are used for the elastic-plastic stress analysis of rolling contact: semi-analytical methods and finite element methods. Elastic solutions serve as the base for the semi-analytical approaches. Boundary conditions are enforced after the completion of a loading cycle while the equilibrium and/or compatibility conditions may be violated during the rolling action [5–9]. The advantage of these models is that many contact cycles can be simulated and advanced constitutive material models can be utilized. While the semi-analytical methods are powerful and attractive, an apparent shortcoming is the accuracy of the results for the rolling contact cases when large plastic deformation develops. In addition, these methods are generally limited to two-dimensional rolling contact problems.

Elastic-plastic stress analyses of rolling contact using the finite element (FE) methods were conducted by Hahn and his coworkers [11–16], Xu and Jiang [10], and Jiang et al. [17]. Dang Van and Maitournam [18] developed a procedure for the numerical analysis of repeated rolling contact. It was noted that different material models produced drastically different results. For example, the FE simulation with a linear kinematic plasticity model predicted a ''forward'' surface movement [11,19] for pure line rolling contact while the FE analysis with a two-surface plasticity model produced a ''backward'' flow [16]. The residual stresses obtained based on different plasticity theories also differed significantly. Experimental observations have established that a pure line rolling contact produces a ''forward'' surface movement and the progressive surface flow decays with increasing number of rolling passes [20,21]. All of the FE simulations except those by Jiang et al. [17] and Xu and Jiang [10] predicted either zero stabilized surface movement or constant rate surface movement.

Very limited work has been done in the elastic-plastic stress analysis of three-dimensional rolling contact using the FE method. Kulkarni et al. [22–24] conducted elastic-plastic stress analyses of three-dimensional rolling contact. Pure rolling with a circular contact patch was analyzed. No elastic-plastic finite element analysis of three-dimensional rolling contact has been conducted for the cases with tangential forces on the contact area. The tangential forces greatly influence the rolling contact stress and failure. For line rolling contact problems, when the shear traction is over 0.25 of the normal pressure, the maximum shear stress occurs on the contact surface, and the maximum shear stress becomes a strong function of the tangential force.

In addition, an accurate elastic-plastic stress analysis of rolling contact depends critically on the material constitutive model used. Use of an unsuited material model for complicated stress state and loading history may result in theoretical simulations qualitatively and quantitatively different from experimental observations. Rolling contact stress represents one of the most complicated of those encountered in engineering applications. The stress state is three-dimensional and the loading history is nonproportional with rotating maximum shear planes. This requires a realistic material model in the elastic-plastic stress analysis. However, some important cyclic plasticity phenomena were explored extensively

Contributed by the Tribology Division for publication in the ASME JOURNAL OF TRIBOLOGY. Manuscript received by the Tribology Division April 19, 2001; revised manuscript received April 3, 2002. Associate Editor: C. H. Venner.

only in the past decade. For example, cyclic ratchetting is a progressive and directional accumulation of strain in an asymmetric stress-controlled material experiment. Most metallic materials display ratchetting rate decay; i.e., the ratchetting strain rate decreases with increasing number of loading cycles. Most existing plasticity models cannot properly describe the experimentally observed ratchetting behavior [25–28]. An inherent shortcoming of the plasticity models used by Hahn and his co-workers [11–16,19,22–24] in their FE simulations is the inability of the material models to consider the ratchetting deformation of the materials.

The current investigation is a study of the three-dimensional rolling contact problems above the plastic shakedown limit using the FE method with the consideration of shear traction in both rolling and lateral directions.

2 Three-Dimensional Rolling Contact

Coordinates System. As a first effort, the study was devoted to the three-dimensional rolling with a circular contact area (Fig. 1) with the normal pressure following the Hertzian distribution,

$$p = p_0 \sqrt{1 - \left(\frac{x}{a}\right)^2 - \left(\frac{y}{a}\right)^2} \tag{1}$$

where a is the radius of the contact area. The maximum Hertzian pressure is denoted by p_0. In the following discussions, P is used to denote the total normal pressure over the circular contact area with a radius of a. The total shear force in the longitudinal (x) direction is Q_x and the total shear force in the lateral (y) direction is Q_y (see Fig. 1). The shear force distributions over the contact area are assumed to be proportional to the normal pressure. In other words, no stick-slip (partial slip) conditions are considered. The contact load moves in the x-direction.

Elastic Shakedown. Elastic shakedown is the limit below which plastic deformation will not occur for rolling contact loading. This is also called the first yield [1]. The elastic shakedown condition can be mathematically expressed as,

$$MAX\left\{\sqrt{\frac{1}{2}\tilde{S}:\tilde{S}}\right\} = k \tag{2}$$

where $\tilde{S}$ represents the deviatoric stress tensor, and k is the yield stress in shear of the material. A colon between two tensors denotes their inner product. *MAX* in the equation is taken with respect to all the material points in the rolling element.

Plastic Shakedown. When the rolling load is above the elastic shakedown limit, plastic deformation occurs. However, when the loading magnitude is above the elastic shakedown but below a certain level, plastic deformation will disappear after a limited number of rolling passes. This loading limit is called plastic shakedown. Cyclic plasticity persists when the rolling load is above the plastic shakedown limit. Results and extensive discussions about shakedown limits can be found in references [1], [29–31].

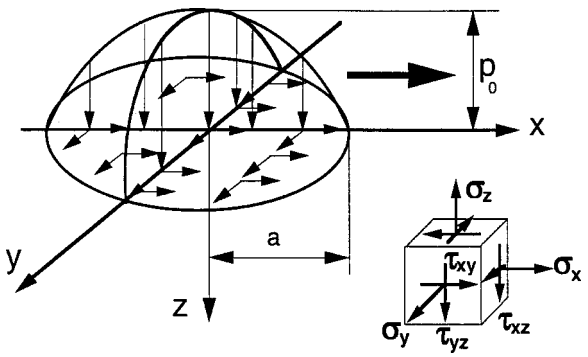

Fig. 1 Three-dimensional rolling contact: coordinates system

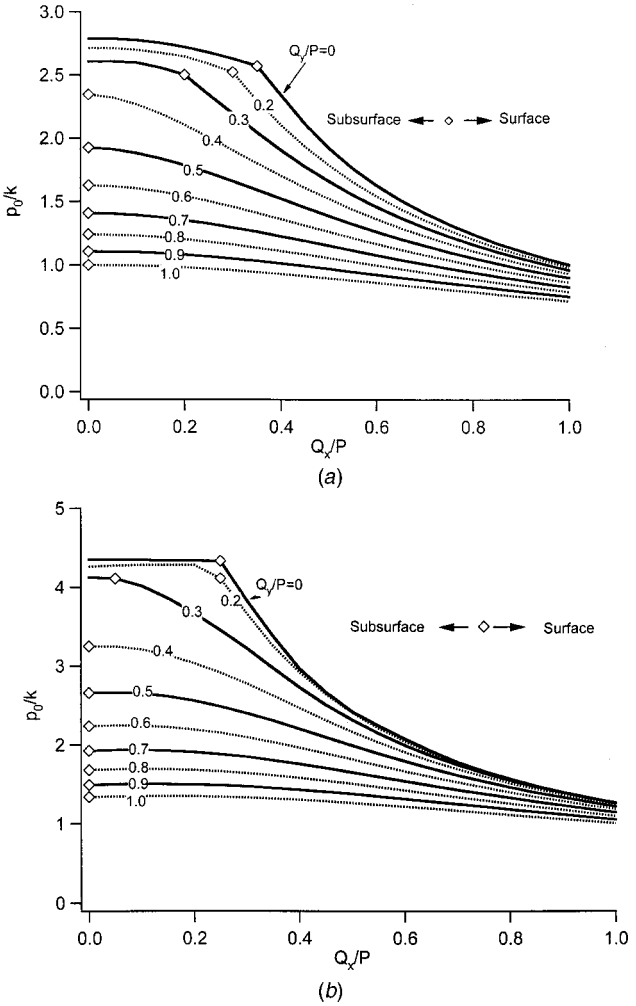

Fig. 2 Shakedown limit for the three-dimensional rolling contact with a circular contact patch: (*a*) elastic shakedown limit; and (*b*) plastic shakedown limit.

Mathematically, an equivalent stress magnitude can be defined as follows [32],

$$\overline{\sigma_a} = MIN\left\{MAX\left[\sqrt{\frac{3}{2}(\tilde{S}-\tilde{S}^0):(\tilde{S}-\tilde{S}^0)}\right]\right\}, \tag{3}$$

where $\tilde{S}^0$ represents a point in the deviatoric stress space. Maximum is taken with respect to the points $\tilde{S}$ in the loading path for a given $\tilde{S}^0$ and minimum is taken in terms of all the possible $\tilde{S}^0$. The principle is to find a center of a circle in the deviatoric space so that the maximum distance to the loading path is a minimum. In other words, there is a smallest circle that circumscribes the loading path in the deviatoric stress space. The radius of this smallest circle is defined as the equivalent stress amplitude for the loading path. This circle can be determined computationally.

When the maximum equivalent stress amplitude under rolling contact is equal to the yield stress of the material, a threshold is reached. This threshold is the plastic shakedown limit [31]. Therefore, the plastic shakedown condition is:

$$MAX\{\overline{\sigma_a}\} = \sqrt{3}k \tag{4}$$

MAX in the equation is taken with respect to all the material points in the rolling element.

Analytical solutions for the elastic rolling contact stresses are available from the literature [3,4]. The elastic shakedown limits for various combinations of Q_x/P and Q_y/P are shown in Fig. 2(*a*). The diamond markers in the figure represent the demarcation of the locations where plastic deformation will first occur either subsurface or on the surface. Figure 2(*b*) shows the plastic shakedown limits for the rolling contact with combined shear traction. The diamond markers provide a demarcation between the conditions for the persistent cyclic plastic deformation to occur subsurface or on contact surface. Clearly, the increase in the shear traction will move the location of the maximum cyclic plastic deformation to the contact surface.

Under the pure rolling contact condition (no tangential forces), initial plastic deformation occurs when the p_0/k ratio is larger than 2.79 for the three-dimensional rolling contact with a circular contact patch (see Fig. 2(*a*)). Persistent cyclic plastic deformation occurs when the p_0/k ratio is larger than 4.26 (see Fig. 2(*b*)). Clearly, the plastic shakedown limits are much higher than the elastic shakedown limits.

It should be noted that the results presented in Fig. 2 for the shakedown limits are independent of materials. Due to the nature of the shakedown phenomenon, the determination of both the elastic and plastic shakedown limits is purely based on elastic calculations. The elastic shakedown limits are symmetric in terms of shear traction in the *x* and *y* directions. That is, if the conditions for an elastic shakedown limit are $p_0/k=2.1$, $Q_x/P=0.2$, $Q_y/P=0.4$, then $p_0/k=2.1$, $Q_x/P=0.4$, $Q_y/P=0.2$ also represent an elastic shakedown limit. However, this symmetry does not apply to the plastic shakedown as can be found from the results shown in Fig. 2(*b*). This is due to the path-dependence of plastic deformation.

3 Cyclic Plasticity Model

The material is assumed to be homogeneous and initially isotropic. For small deformation the total strain can be decomposed additively into the elastic and plastic parts. For the elastic part, the Hooke's law is valid, i.e.,

$$\tilde{\sigma}=\tilde{\tilde{C}}:\tilde{\varepsilon}^e=\tilde{\tilde{C}}:(\tilde{\varepsilon}-\tilde{\varepsilon}^p) \tag{5}$$

where $\tilde{\sigma}$ is the stress tensor, $\tilde{\varepsilon}^e$ is the elastic strain tensor, $\tilde{\varepsilon}^p$ is the plastic strain tensor, and $\tilde{\tilde{C}}$ is the elasticity modulus tensor. Single and double tildes above a letter designate a second order and a fourth order tensors, respectively.

The von Mises yield function and the associated flow rule are used:

$$f=\sqrt{(\tilde{S}-\tilde{\alpha}):(\tilde{S}-\tilde{\alpha})}-\sqrt{2}k=0 \tag{6}$$

$$d\tilde{\varepsilon}^p=\frac{1}{h}\langle d\tilde{S}:\tilde{n}\rangle\tilde{n} \tag{7}$$

where,

$$\tilde{n}=\frac{\partial f}{\partial(\tilde{S}-\tilde{\alpha})}=\frac{\tilde{S}-\tilde{\alpha}}{\sqrt{(\tilde{S}-\tilde{\alpha}):(\tilde{S}-\tilde{\alpha})}} \tag{8}$$

The symbol f represents the yield surface, $\tilde{\alpha}$ is the backstress tensor in the deviatoric space representing the center of the yield surface, and k is the yield stress in simple shear. The prefix d denotes infinitesimal increment. The symbol $\tilde{n}$ is the unit normal on the yield surface. The symbol $\langle\,\rangle$ represents the Macauley bracket (i.e., $\langle x\rangle=0.5(x+|x|)$) and h is a scalar function often called the plastic modulus function. The quantity dp is generally called the equivalent plastic strain increment and is defined as,

$$dp=\sqrt{d\tilde{\varepsilon}^p:d\tilde{\varepsilon}^p} \tag{9}$$

A hardening rule specifies changes in the yield condition as a result of loading the material. Following Chaboche et al. [33], the total backstress is decomposed into a number of additive parts,

$$\tilde{\alpha}=\sum_{i=1}^{M}\tilde{\alpha}^{(i)} \tag{10}$$

where $\tilde{\alpha}^{(i)}(i=1,2,\ldots,M)$ represent backstress parts, and M is an integer representing the number of backstress parts.

Chaboche et al. [33–35] generalized the hardening rule developed by Armstrong and Frederick [36]. Ohno and Wang [37–40] proposed a threshold term in the hardening rule to limit the predicted ratcheting rate. The Ohno-Wang model provides a close prediction for the experimental observations [27,28]. Jiang and Sehitoglu [41,42] and Ohno and Wang [43] modified the Chaboche model further and the resulted model improves the prediction of cyclic stress-strain responses of a material under general multiaxial and nonproportional loading conditions. The mathematical expression for the hardening rule in the recently developed plasticity model [41] is,

$$d\tilde{\alpha}^{(i)}=c^{(i)}r^{(i)}\left(\tilde{n}-\left(\frac{\|\tilde{\alpha}^{(i)}\|}{r^{(i)}}\right)^{\chi^{(i)}+1}\frac{\tilde{\alpha}^{(i)}}{\|\tilde{\alpha}^{(i)}\|}\right)dp \quad (i=1,2,\ldots,M) \tag{11}$$

where $c^{(i)}$, $r^{(i)}$, and $\chi^{(i)}$ $(i=1,2,\ldots,M)$ are material constants and,

$$\|\tilde{\alpha}^{(i)}\|=\sqrt{\tilde{\alpha}^{(i)}:\tilde{\alpha}^{(i)}} \quad (i=1,2,\ldots,M) \tag{12}$$

In the context of this paper, the material properties considered will be representative of cyclically stable response. Details of the cyclic plasticity model and the determination of the material constants can be found in references [25], [41], [42], [44].

The three-dimensional stress state in rolling contact is one of the most complicated in engineering. Both mean stress relaxation and strain ratchetting occur in rolling contact. It is clear that if a cyclic plasticity model is not able to describe the cyclic plasticity phenomenon under a simple stress state and loading history, the model is not suitable for the elastic-plastic stress analysis for such complicated problems as rolling contact. The cyclic plasticity model presented in this section has been applied to the predictions of long-term ratchetting of 1070 steel under various proportional and nonproportional loading conditions. Very good agreement was achieved between predictions and experiments. Detailed demonstrations of its capability to predict stress-strain responses for general multiaxial and nonproportional loading can be found in references [25–28], [32], [41], [42], [44].

4 Finite Element Model

The cyclic plasticity model described in the last section was implemented into an FE code. A backward Euler algorithm is used in an explicit stress update algorithm. The algorithm reduces the plasticity model into a nonlinear equation that can be solved by the Newton method. The corresponding consistent tangent operator is derived for the global equilibrium iteration, which ensures the quadratic convergence of the global Newton-Raphson equilibrium iteration procedure. Detailed formulation for the implementation of the material model is presented in Appendix A.

Finite Element Mesh. Due to the nature of the three-dimensional rolling contact, no symmetry can be found. Therefore, a general three-dimensional model had to be created. A quarter of the finite element (FE) mesh is shown in Fig. 3. 20-node quadric brick elements were used. Fine mesh with a size of $0.24a$ was used in the middle of the contact area where a is the radius of the circular contact area (refer to Fig. 1). There were a total of 2354 brick elements with a total of 11030 nodes in the model for a volume of $24a\times6a\times6a$. In addition, there were 116 infinite elements used in the boundaries other than the rolling contact surface (refer to Fig. 3). The infinite elements were employed to simulate the space far from the area of contact. Rolling con-

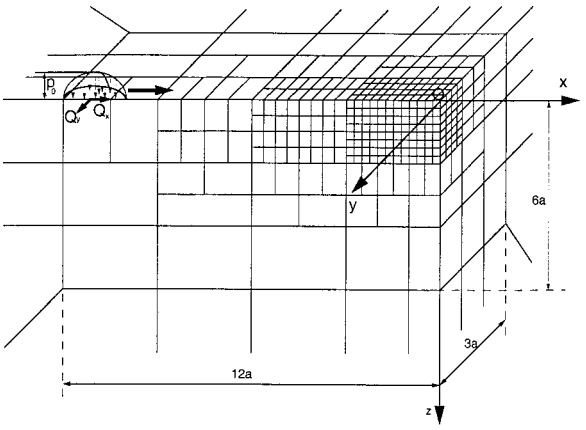

Fig. 3 Finite element mesh for the three-dimensional rolling contact

tact generally results in very localized plastic deformation. The use of infinite elements greatly facilitates the rolling contact stress analysis.

The contact loading was modeled by applying concentrated node forces as a time-dependent amplitude function. The contact load was increased gradually on the left side of the contact region until it reached the desired value. A total of 10 incremental steps were used for the indentation. After applied, the contact load translated in the rolling (x) direction step by step for a distance of $22a$ until it reached the right side of the contact region. Depending on the loading magnitude, a total of 120~400 incremental steps were taken to translate the contact load over a distance of $22a$. The maximum increment step length used was $0.18a$. After it reached the far right end, the contact load was decreased gradually in 10 incremental steps until it became zero. One rolling pass was completed at this point. This procedure was repeated for six rolling passes for each loading case simulated in this investigation.

In idealized rolling contact, any material points with identical y and z coordinates have identical stress and strain responses. In other words, the residual stresses and strains are independent of the x coordinate. In the FE simulations, the aim was to obtain the stress and strain responses for the middle cross section (yOz) (refer to Fig. 3). It is hoped that the stress and strain results near the yOz cross section are accurate. The results in the rest of the area are approximate.

Material Constants. The material properties of the 1070 steel with a fully pearlitic structure [9] were used for the rolling contact simulations. The material constants used in the cyclic plasticity material model are list in Table 1. 1070 steel is widely used for rails and wheels.

5 Finite Element Results

Four loading cases were simulated. Each case had a p_0/k ratio of 6.0, where p_0 is the peak Hertzian pressure in the rolling contact (refer to Fig. 1) and k is the yield stress in shear of the material. A pure rolling without shear traction was simulated to serve as a base for comparison. The other three cases had a Q_y/P ratio of 0.25, where Q_y is the total shear force in the lateral (y) direction and P is the total normal pressure. The difference among these three loading cases was the Q_x/P ratio, where Q_x is the total shear force in the rolling (x) direction on the circular contact surface. These three Q_x/P ratios were 0.2, 0.4, and 0.6, respectively. In addition, a two-dimensional pure rolling contact was analyzed and the results obtained were used to compare with those from the three-dimensional analyses.

Table 1 Material constants used in plasticity model

E=210 GPa, μ=0.3, k=100MPa, M=5
$c^{(1)}$=16323, $c^{(2)}$=493, $c^{(3)}$=149, $c^{(4)}$=45, $c^{(5)}$=13.6
$r^{(1)}$=120.5 MPa, $r^{(2)}$=76.3MPa, $r^{(3)}$=89.6MPa, $r^{(4)}$=100.4MPa, $r^{(5)}$=152.5 MPa
$\chi^{(1)}$= $\chi^{(2)}$= $\chi^{(3)}$= $\chi^{(4)}$= $\chi^{(5)}$=5

All the finite element simulations were conducted using an SGI Origin 2000 computer at the National Center for Supercomputing Applications (NCSA) at the University of Illinois at Urbana-Champaign. Due to the inherent difficulty caused by the large amount calculations involved in the three-dimensional elastic-plastic rolling contact stress analysis, a limited number of rolling passes can be simulated within a realistic period time. In this investigation, six rolling passes were simulated for each loading scenario. CPU times were dependent on the degree of cyclic plasticity involved under a given rolling condition. The ($p_0/k=6$, $Q_x/P=0.6$, $Q_x/P=0.25$) case resulted in the largest cyclic plasticity among all the loading cases studied. The CPU time to complete one rolling pass for this case was approximately 120 CPU hours. For the other loading cases, the CPU time was approximately 50 hours per rolling pass.

Normalized quantities are used in reporting the results. The length is normalized in terms of the radius of the circular contact area, a, the stresses are normalized by the yield stress in shear, k, the shear strains are normalized by k/G, and the surface movement is normalized by ka/G, where G is the shear elasticity modulus. All the results reported below were taken from the middle cross section yOz (refer to Fig. 3).

All the six residual stress components (normal and shear stresses) and six residual strain components are non-zero for the three-dimensional rolling contact. However, the residual stress in the z direction, all the three shear residual stresses, the three normal residual strains, and the residual strain component $(\gamma_{xy})_r$ are not significant as compared to the rest of the stress and strain components. Therefore, these less significant quantities will not be reported.

Rolling Case $p_0/k=6$, $Q_x/P=0.4$, $Q_y/P=0.25$. The development of residual stresses in the x and y directions on the along the z axis is shown in Fig. 4 for the ($p_0/k=6$, $Q_x/P=0.4$, $Q_y/P=0.25$) loading case. The residual stresses are compressive on the contact surface and also subsurface near the contact surface. Tensile residual stresses are found subsurface when $z/a>1$ for the y direction and when $z/a>1.5$ for the x direction. The maximum (absolute value) residual stress in the x direction occurs on the contact surface. The maximum residual stress in the y direction occurs subsurface at $z/a=0.5$ and the value is approximately 50 percent of the yield stress in shear of the material. The value of the residual stress in the y direction is substantially smaller than that in the x direction for the loading case considered.

For three-dimensional rolling contact, the residual stresses are independent of x coordinate for an idealized rolling contact but they are functions of the y coordinate. Figures 5 displays the residual stress profile in terms of y coordinate for the x direction after six rolling passes. It can be found that with a tangential force $Q_x/P=0.4$ in the rolling (x) direction and a tangential force $Q_y/P=0.25$ in the lateral (y) direction, maximum residual stresses occur at a y coordinate near zero. It is noted that the residual stress in the x direction on the contact surface is positive at $y/a=-1$. It should be also noted that the maximum residual stresses generally occur at locations different from $y=0$ for the three-dimensional rolling contact problem considered. However, the maximum residual stresses are not significantly different from the value at $y=0$. Therefore, residual stresses at $y=0$ are reported.

Development of two residual shear strain components with the rolling cycles is shown in Fig. 6 along the z axis. Under the

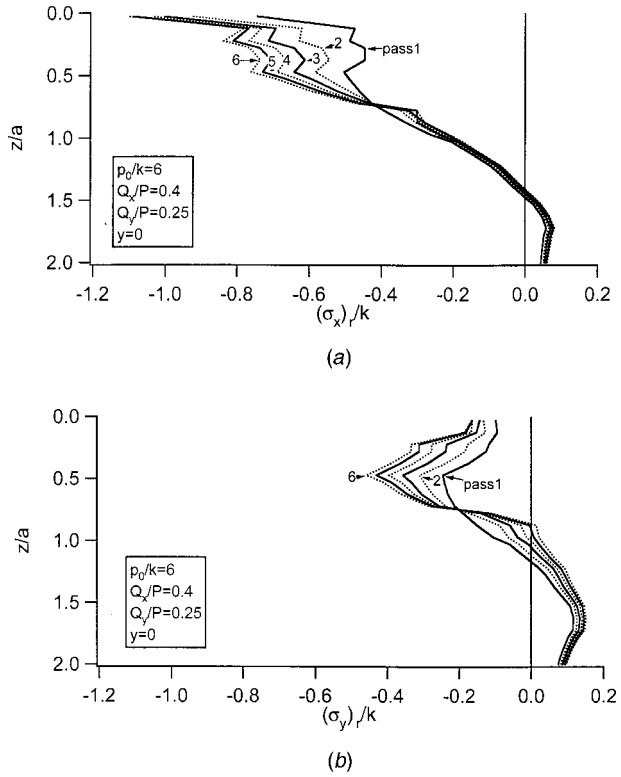

Fig. 4 Development of residual stresses for $p_0/k=6.0$, $Q_x/P=0.4$, $Q_y/P=0.25$, $y=0$: (*a*) *x*-direction; and (*b*) *y*-direction.

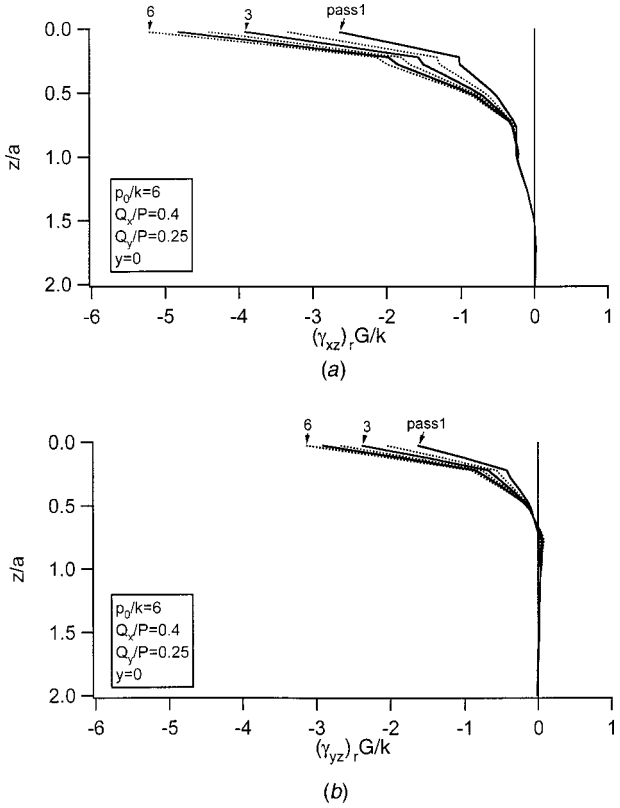

Fig. 6 Development of residual shear strains for $p_0/k=6.0$, $Q_x/P=0.4$, $Q_y/P=0.25$, $y=0$: (*a*) $(\gamma_{xz})_r$; and (*b*) $(\gamma_{yz})_r$.

coordinate system employed, both of the residual shear strains are negative in value. It should be noted that all the shear strain values are multiplied by G/k in the presentation. The maximum values of the residual shear strains occur on the surface. The residual shear strain $(\gamma_{xz})_r$ is approximately twice as large as the residual shear strain $(\gamma_{yz})_r$. The residual shear strain $(\gamma_{xz})_r$ contributes to the surface displacement in the x direction and the residual shear strain $(\gamma_{yz})_r$ results in the surface movement in the y direction.

Figures 7 shows the residual shear strain profile after six rolling cycles for $(\gamma_{xz})_r$ with respect to the y coordinate. The residual shear strain $(\gamma_{xz})_r$ is negative in value under the coordinate system employed. It is minimal in the locations outside of the contact area.

The surface displacements in the x direction are summarized in Fig. 8 with respect to the y coordinate for the first six rolling cycles. The displacement in the x direction is the largest when $y=0$. The displacement increases with increasing number of rolling passes. However, the rate of surface displacement decays as the

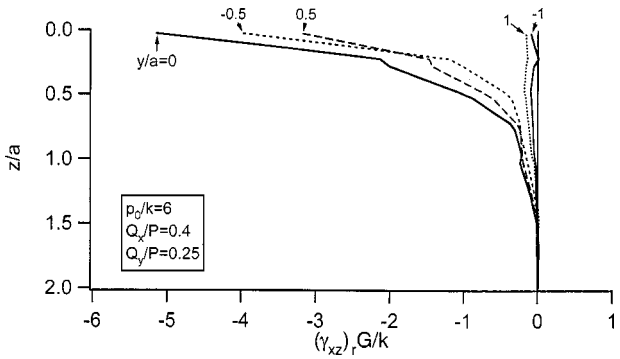

Fig. 7 Residual shear strain $(\gamma_{xz})_r$ profile for $p_0/k=6.0$, $Q_x/P=0.4$, $Q_y/P=0.25$ after six rolling passes

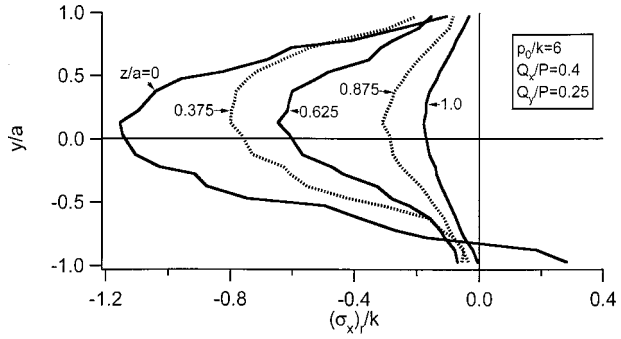

Fig. 5 Profile of the residual stress in the *x*-direction after six rolling passes for $p_0/k=6.0$, $Q_x/P=0.4$, and $Q_y/P=0.25$

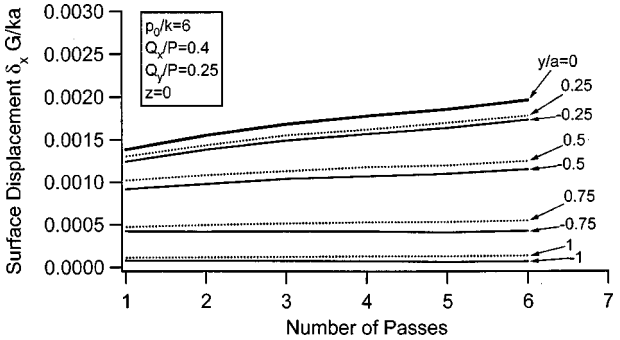

Fig. 8 Surface displacement in the *x*-direction for $p_0/k=6.0$, $Q_x/P=0.4$, and $Q_y/P=0.25$

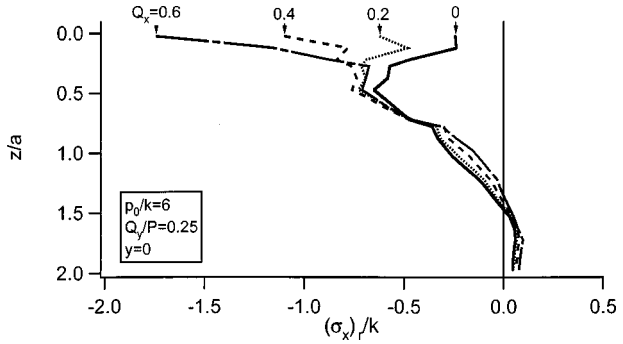

Fig. 9 Influence of tangential force Q_x on the residual stress in the x-direction ($p_0/k=6.0$, $Q_y/P=0.25$, after six cycles)

rolling passes increase. This is in agreement with the general experimental observation on the surface displacement [20–21]. It is noted that the displacement in the x direction is not symmetric with respect to the y coordinate due to the application of the lateral shear traction. The surface displacement is a result of the residual shear strain beneath the contact surface. It can be obtained by integrating the residual shear strain with respect to z. In the FE analysis, the surface displacement was obtained directly from the simulations.

It should be mentioned again that all the six residual stress and six residual strain components are non-zero for the three-dimensional rolling contact. However, some of the residual stress and strain components are small as compared to the others. The two reported residual stress components and the two residual shear strain components represent the most significant among all the 12 stress and strain components.

Influence of Tangential Shear Conditions. The tangential condition has a significant influence on the residual stresses and residual strains for the three-dimensional rolling contact. Figures 9 and 10 summarize the influence of the Q_x/P ratio on the residual stresses and residual strains. The four loading cases had a p_0/k ratio of 6.0 and a Q_y/P ratio of 0.25. The results were taken from the z-axis after six rolling passes.

In Fig. 9 the residual stresses in the x direction are shown for different shear traction conditions. Clearly, all the residual stresses in the x direction are compressive for the material near the contact surface. The increase of the tangential force Q_x results in an increase of compressive residual stress in the x direction in the thin layer of material near the contact surface. The thickness of this layer of material is approximately $0.5a$. Maximum (absolute value) residual stress in the x direction occurs on the contact surface when the Q_x/P ratio is larger than 0.2.

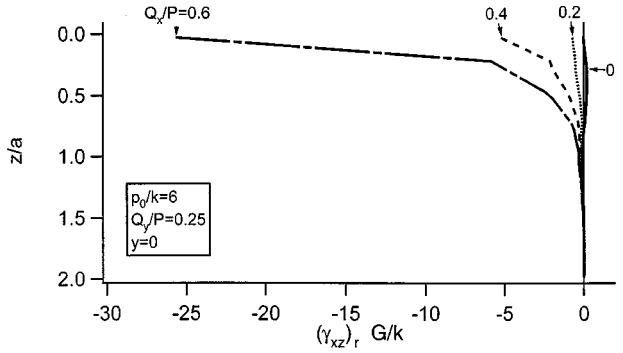

Fig. 10 Influence of tangential force Q_x on the residual shear strain $(\gamma_{xz})_r$ ($p_0/k=6.0$, $Q_y/P=0.25$, after six cycles)

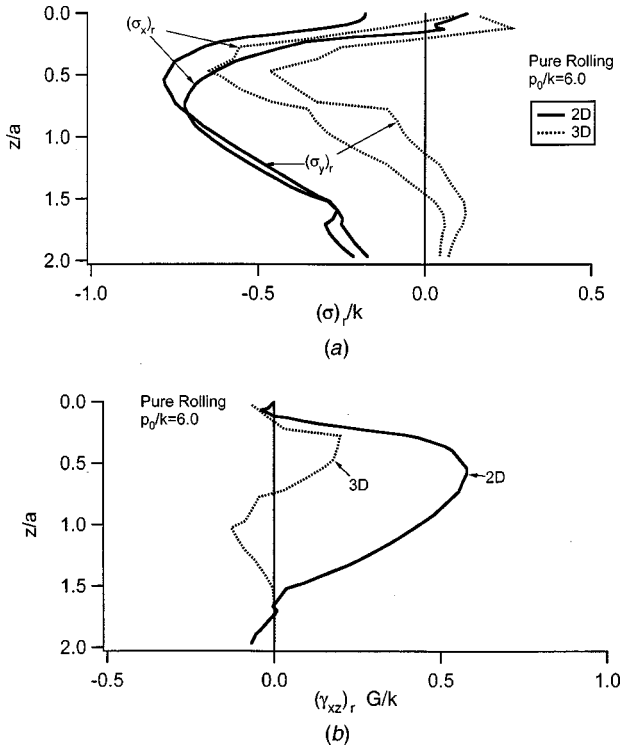

Fig. 11 Comparison of the residual stresses and stain for the two-dimensional and three-dimensional pure rolling ($p_0/k=6.0$, after six rolling passes): (*a*) residual stresses; and (*b*) residual shear strain $(\gamma_{xz})_r$.

Figures 10 exhibits the influence of the tangential forces on the residual strains $(\gamma_{xz})_r$. It can be found that the tangential force Q_x has a very significant influence on the residual strain. The residual strain near the contact surface increases exponentially with the tangential force. Maximum residual shear strain occurs on the contact surface when Q_x/P ratio is equal to or larger than 0.2. For the four loading scenarios under investigation, the residual strain $(\gamma_{xz})_r$ is about twice as large as $(\gamma_{yz})_r$ on the contact surface. For the load case with $Q_x/P=0$, the residual shear strain $(\gamma_{xz})_r$ is positive subsurface, although the magnitude is very small as compared to the residual strain values of the other three loading cases. The three loading conditions with non-zero Q_x/P ratio result in negative residual strains under the coordinate system employed. Noting that $(\gamma_{xz})_r$ contributes to the surface movement in the x direction and a negative surface displacement is a ''backward'' surface movement in terms of the direction of rolling, the three case with non-zero Q_x/P ratios are predicted to result in ''backward'' surface movement in the rolling direction.

The Q_x/P ratio has a much larger influence on the residual stress in the x direction than in the y direction. It has a much significant influence on $(\gamma_{xz})_r$ than on $(\gamma_{yz})_r$.

Pure Rolling Contact. It will be useful to compare the results of the two-dimensional (line) pure rolling and the three-dimensional pure rolling contact. Pure rolling refers to the rolling contact without surface shear traction. The results of the residual stresses and residual shear strain for the pure line rolling contact (two-dimensional pure rolling) and three-dimensional pure rolling contact with identical p_0/k ratio after six rolling passes are presented in Fig. 11. The three-dimensional pure rolling has a circular contact area.

The residual stresses in the x direction are similar for both the three-dimensional and two-dimensional pure rolling. Both pure rolling cases result in a small tensile residual stress $(\sigma_x)_r$ on the contact surface. The maximum residual stress in the x direction is

higher for the two-dimensional pure rolling. The residual stress in the y direction is very different for the two pure rolling cases (Fig. 11(a)). For the two-dimensional pure rolling, the residual stresses in the y direction are all compressive. The three-dimensional pure rolling results in a tensile residual stress in the y direction for the material near the contact surface. The maximum magnitude of the residual stress in the y direction for the three-dimensional pure rolling is significantly smaller than that of the two-dimensional pure rolling. This implies that the residual stresses are not as protective in the three-dimensional loading compared with the corresponding two-dimensional case.

The residual shear strain $(\gamma_{xz})_r$ is also very different for the two pure rolling cases (Fig. 11(b)). The two-dimensional pure rolling produces positive residual shear strain $(\gamma_{xz})_r$. The three-dimensional pure rolling results in both positive and negative residual shear strain $(\gamma_{xz})_r$. According to the coordinate system employed, a positive contributes to a ''forward'' surface displacement. Therefore, the two-dimensional pure rolling produces a ''forward'' surface movement. The three-dimensional pure rolling is also predicted to produce a ''forward'' surface displacement, but the magnitude of the surface movement in the x direction for the three-dimensional pure rolling is significantly smaller than that of a two-dimensional pure rolling.

The residual shear strain component $(\gamma_{yz})_r$ is zero for the pure line contact. In the three-dimensional pure rolling contact with a circular contact area, this shear strain component is not zero. However, the shear strain component γ_{yz} is insignificant as compared to the shear strain component γ_{xz}. In fact, the maximum residual shear strain $(\gamma_{yz})_r$ is $0.04G/k$ for the three-dimensional pure rolling under consideration after six rolling passes while the maximum residual shear strain $(\gamma_{xz})_r$ is $0.2G/k$ (refer to Fig. 11(b)).

In summary, with an identical p_0/k ratio the two-dimensional pure rolling (pure line rolling) produces larger plastic deformation than the three-dimensional pure rolling with a circular contact patch. As a result, the two-dimensional pure rolling produces larger residual stresses and residual strains. Both pure rolling cases produce a ''forward'' surface movement. However, the two-dimensional pure rolling is expected to result in much larger surface movement than the three-dimensional pure rolling. It is therefore anticipated that the two-dimensional pure rolling contact will have a shorter service life than the three-dimensional pure rolling.

6 Discussions

The current investigation was concentrated on the influence of the surface shear traction on the three-dimensional rolling contact. Several simplifications were made. The elasticity based Hertzian distribution was assumed for the normal surface contact load. When the contact load exceeds the elastic shakedown limit, the contact pressure is expected to be different from the Hertzian. In reality the contact area is generally not in a circular shape. It is also well known that partial slip often occurs in the contact area. Further studies need to address these influences.

The results of the FE simulations indicate that more than six rolling passes are needed in order for the residual stresses to stabilize. As was stated in the last section, the three-dimensional elastic-plastic rolling contact stress analysis is time-consuming. However, a stabilized residual stress is expected after a finite number of rolling passes. The asymptotic nature of the residual stress development can be noted from the FE results shown in the last section. A two-dimensional finite element analysis [17] reveals that the residual stresses stabilize after about 30 rolling passes for 1070 steel, and the development of residual stresses appears in an asymptotic nature. The values of the residual stresses after tenth and twentieth rolling cycles were found to be 8 percent and 3 percent less than the stabilized value, respectively [17]. Therefore, the residual stress results obtained for the limited number of rolling passes can be extrapolated to obtain the stabilized residual stress values using an asymptotic function. The residual strains do not stabilize but display long-term ratchetting behavior. It was found that a power-law relationship exists between the residual strain and the number of rolling passes for the constant-amplitude rolling contact [10,17]. It can be expected that such a relationship is also valid for three-dimensional rolling contact. Therefore, the residual strain results obtained for limited number of rolling passes can be extrapolated to longer rolling cycles.

Because the results obtained for the Gauss points were reported in the paper, it should be born in mind that the results reported to be on the $y=0$ plane were actually taken from the Gauss points with a y coordinate of $0.028a$. The same rule applies to the results for the contact surface. All the residual stress and strain results on the contact surface reported in this paper were taken from the Gauss points nearest the contact surface. The z coordinate for these Gauss points of the elements containing the contact surface was also $0.028a$. For the loading cases which do not result in high stress and strain gradients near the contact surface, the values of the Gauss points nearest the contact surface are representative of the stresses and strains on the surface. However, when the stress and strain gradients are high, such as in the cases with high tangential surface traction, the stress and strain values on the contact surface will be higher than those reported.

The detailed stress and strain histories can be used to assess the failure of a rolling component. Multiaxial failure models such as that used by Jiang and Sehitoglu [45] can be used to determine the fatigue damage and ratchetting damage. A failure analysis can be therefore conducted to predict the service life of a rolling component.

The current finite element simulations are meaningful in the cases such as the rail/wheel contact in a curved track where lateral traction is inevitable. The results from the current investigation showed that lateral traction combined with longitudinal traction may produce severe conditions such that the excessive accumulated ratchetting deformation can result in premature failure.

7 Conclusions

Based on a kinematic material hardening concept, shakedown limit results were obtained for the three-dimensional rolling contact with shear traction in both the rolling direction and the lateral direction. The plastic shakedown limits showed that the pressure for shakedown decreases dramatically with increasing shear traction.

The influence of the tangential surface traction on the rolling contact stress was studied using the finite element method. The three-dimensional elastic-plastic stress analysis reveals that the shear traction has a significant influence on the residual stresses and strains on the material near the contact surface. The enhanced plasticity introduced by the surface shear traction will accelerate the failure and/or wear of a rolling element. Due to the use of an advanced cyclic plasticity material model, the rolling contact stress results obtained for repeated rolling are expected to be more realistic than the existing rolling contact stress analyses.

Acknowledgments

The authors would like to thank the financial support from the Association of American Railroads. Computer support was obtained with grants from NCSA at University of Illinois. Discussions with Professor N. Ohno and Dr. M. Kobayashi at the Nagoya University on the implementation of the plasticity model into the finite element package were helpful.

Nomenclature

a = radius of the circular contact area

$\tilde{\tilde{C}}$ = elasticity modulus tensor

$c^{(i)}$, $r^{(i)}$, $\chi^{(i)}$ = material constants in the plasticity model ($i=1,2,\ldots,M$)

d = prefix denoting increment or differentiation

E = Young's modulus
G = shear modulus
f = yield surface function
h = plastic modulus function
$\tilde{\tilde{I}}$ = fourth order unit tensor
k = yield stress in simple shear
$\tilde{1}$ = second order unit tensor
M = positive integer
$\tilde{\mathbf{n}}$ = unit exterior normal to the yield surface at the stress state
p = equivalent plastic strain
P = total normal load
p_0 = maximum Hertzian pressure
Q_x = total tangential force in the rolling direction
Q_y = total tangential force in the lateral direction
$\tilde{\mathbf{S}}$ = deviatoric stress tensor
$\tilde{S}^0$ = center of a surface in the deviatoric space
$\tilde{\alpha}$ = total backstress tensor
$\tilde{\alpha}^{(i)}$ = i^{th} backstress tensor ($i=1,2,\ldots,M$)
$\tilde{\varepsilon}$ = strain tensor
$\tilde{\varepsilon}^e$ = elastic strain tensor
$\tilde{\varepsilon}^p$ = plastic strain tensor
δ_x = surface displacement in the rolling direction
δ_y = surface displacement in the lateral direction
$\tilde{\sigma}$ = stress tensor
σ_x, σ_y, σ_z, τ_{xy}, τ_{xz}, τ_{yz} = orthogonal stress components
σ_a = equivalent stress magnitude
$(\sigma_x)_r$, $(\sigma_y)_r$, $(\sigma_z)_r$, $(\tau_{xy})_r$, $(\tau_{xz})_r$, $(\tau_{yz})_r$ = residual stress components
ε_x, ε_y, ε_z, γ_{xy}, γ_{xz}, γ_{yz} = orthogonal strain components
$(\varepsilon_x)_r$, $(\varepsilon_y)_r$, $(\varepsilon_z)_r$, $(\gamma_{xy})_r$, $(\gamma_{xz})_r$, $(\gamma_{yz})_r$ = Residual strain components
μ = Poisson's ratio
${}^0(\,)$ = state and internal variables in the last increment step

Appendix A

Implementation of the Cyclic Plasticity Model Into Finite Element Code. The plasticity model discussed in Section 3 was implemented into the general purpose FE package ABAQUS [46] through the user-defined subroutine UMAT. A backward Euler algorithm was used in an explicit stress update algorithm. The algorithm reduces the plasticity model into a nonlinear equation that can be solved by Newton's method. The corresponding consistent tangent operator is derived for the global equilibrium iteration, which ensures the quadratic convergence of the global Newton-Raphson equilibrium iteration.

Explicit Stress Update Algorithm. In a strain-drive FE analysis procedure, the global equilibrium solution provides the strain history. The stress and internal variables can be then traced through the integration of the cyclic plasticity constitutive equations. For each equilibrium iteration increment step, the values of all the state variables and internal variables in the last increment step t_n obtained from the equilibrium iteration are denoted using a superscript ${}^0(\,)$, i.e.,

$$ {}^0\tilde{\varepsilon}=\tilde{\varepsilon}(t_n),\quad {}^0\tilde{\sigma}=\tilde{\sigma}(t_n),\quad {}^0\tilde{\varepsilon}^p=\tilde{\varepsilon}^p(t_n),\quad {}^0\tilde{\alpha}=\tilde{\alpha}(t_n), $$
$$ {}^0\tilde{\alpha}^{(i)}=\tilde{\alpha}^{(i)}(t_n) \tag{A1} $$

For a given strain increment $d\tilde{\varepsilon}$ at the time interval $dt=t_{n+1}-t_n$, the purpose of the integration procedure is to find the values of the stress and the internal variables at time t_{n+1}, as being denoted by $(\tilde{\varepsilon},\tilde{\sigma},\tilde{\varepsilon}^p,\tilde{\alpha},\tilde{\alpha}^{(i)})$, that satisfy the evolution rule, Eq. (10) and Eq. (11), and the yield criterion, Eq. (6).

The stress and the internal variables can be expressed in terms of the plastic multiplier dp. Since the plastic multiplier is unknown a priori, the material is assumed to deform elastically at first, that is, $dp=0$. This first trial results in the elastic trial values of the variables,

$$ \tilde{\varepsilon}^{tr}={}^0\tilde{\varepsilon}+d\tilde{\varepsilon} \tag{A2} $$

$$ \tilde{\sigma}^{tr}=\tilde{\tilde{C}}:(\tilde{\varepsilon}^{tr}-{}^0\tilde{\varepsilon}^p) \tag{A3} $$

$$ \tilde{\varepsilon}^{p.tr}={}^0\tilde{\varepsilon}^p \tag{A4} $$

$$ \tilde{\alpha}={}^0\tilde{\alpha}\quad\text{and}\quad \tilde{\alpha}^{(i),tr}={}^0\tilde{\alpha}^{(i)}\quad (i=1,2,\ldots,M) \tag{A5} $$

This procedure is called elastic predictor. If these trial values do not violate the yield condition, then they are the solutions at time t_{n+1}. If the yield criterion is violated, the plastic multiplier dp, which determines the other variables, must be positive but unknown.

By integrating the evolution function for the backstress parts, Eq. (11), through the backward Euler scheme, the updated backstress parts $\tilde{\alpha}^{(i)}$ $(i=1,2,\ldots,M)$ can be obtained,

$$ \tilde{\alpha}^{(i)}=\varsigma^{(i)}(c^{(i)}r^{(i)}\tilde{n}\,dp+{}^0\tilde{\alpha}^{(i)})\quad (i=1,2,\ldots,M) \tag{A6} $$

where,

$$ \varsigma^{(i)}=\frac{1}{1+(\|\tilde{\alpha}^{(i)}\|/r^{(i)})^{\chi^{(i)}}c^{(i)}dp}\quad (i=1,2,\ldots,M) \tag{A7} $$

The stress is integrated from the Hooke's law, Eq. (5), together with the flow rule, Eq. (7), and the deviatoric stress $\tilde{S}$ is obtained as follows,

$$ \tilde{S}={}^0\tilde{S}+\tilde{\tilde{C}}:d\tilde{\varepsilon}^{\text{dev}}-2G\,dp\tilde{n} \tag{A8} $$

where G is the shear modulus and $d\tilde{\varepsilon}^{\text{dev}}$ is the deviatoric strain increment.

Let $\tilde{\beta}=\tilde{S}-\tilde{\alpha}$. From Eqs. (10), (A6), and (A8), the following identical equation is satisfied,

$$ \tilde{l}=\tilde{\beta}-{}^0\tilde{S}-\tilde{\tilde{C}}:d\tilde{\varepsilon}^{\text{dev}}+2G\,dp\tilde{n}+\sum_{i=1}^{M}c^{(i)}r^{(i)}\varsigma^{(i)}dp\tilde{n}+\sum_{i=1}^{M}\varsigma^{(i)0}\tilde{\alpha}^{(i)} $$
$$ =0 \tag{A9} $$

Because $\tilde{\beta}=\tilde{S}-\tilde{\alpha}$, the yield criterion, Eq. (6), can be rewritten as,

$$ f=\sqrt{\tilde{\beta}:\tilde{\beta}}-\sqrt{2}k=0 \tag{A10} $$

The unknowns $\tilde{\beta}$ and dp can be obtained from the nonlinear algebraic Eqs. (A9) and (A10) by the Newton method.

The consistently linearized form of Eq. (A9) leads to,

$$ \tilde{l}+\tilde{\tilde{\pi}}:\delta\tilde{\beta}+c_n\tilde{n}\,\delta p+\sum_{i=1}^{M}c_\alpha^{(i)0}\tilde{\alpha}^{(i)}\delta p=0 \tag{A11} $$

The symbols in Eq. (A11) are defined in Appendix B. The prefix δ denotes an increment in the local Newton iteration procedure.

Solving Eq. (A11) by applying the Lemma presented in Appendix C yields,

$$ \delta\tilde{\beta}=-\tilde{\tilde{\pi}}^{-1}:\left(\tilde{l}+c_n\tilde{n}\,\delta p+\sum_{i=1}^{M}c_\alpha^{(i)0}\tilde{\alpha}^{(i)}\delta p\right) \tag{A12} $$

The Newton iteration for the yield Eq. (A10) results in,

$$ f+\tilde{n}:\delta\tilde{\beta}-\frac{\partial k}{\partial p}\delta p=0 \tag{A13} $$

By substituting Eq. (A12) into Eq. (A13), the explicit Newton iteration formulation for dp can be obtained,

$$\delta p_{(j)}=\frac{f_{(j)}-\tilde{n}_{(j)}:\tilde{\tilde{\pi}}_{(j)}^{-1}:\tilde{I}_{(j)}}{D_{(j)}} \tag{A14}$$

where $D_{(j)}=\tilde{n}_{(j)}:\tilde{\tilde{\pi}}_{(j)}^{-1}:(c_{n(j)}\tilde{n}_{(j)}+\Sigma_{i=1}^{M}c_{\alpha(j)}^{(i)}\,{}^{0}\tilde{\alpha}^{(i)})$, and the subscript $(\,)_{(j)}$ denotes the local Newton iteration step.

Once the Newton iteration process for Eq. (*A*14) converges, the plastic multiplier dp takes the value for the last iteration step, the j^{th} step, i.e., $dp=dp_{(J)}$ and $dp_{(j+1)}=dp_{(j)}+\delta p_{j+1}$, $(j=0,1,2,\ldots,J-1)$. Furthermore, the stress and the internal variables are updated following the constitutive equations,

$$\left.\begin{aligned}
\tilde{S}&={}^{0}\tilde{S}+\tilde{\tilde{C}}:d\tilde{\varepsilon}^{\text{dev}}-2Gdp\tilde{n}_{(J)}\\
\tilde{\alpha}&=\sum_{i=1}^{M}\tilde{\alpha}^{(i)},\quad \tilde{\alpha}^{(i)}=\varsigma^{(i)}(c^{(i)}r^{(i)}dp\tilde{n}_{(J)}+{}^{0}\tilde{\alpha}^{(i)})\\
\tilde{n}_{(J)}&=\frac{\partial f}{\partial(\tilde{S}-\tilde{\alpha})}=\frac{\tilde{S}_{(J)}-\tilde{\alpha}_{(J)}}{\sqrt{(\tilde{S}_{(J)}-\tilde{\alpha}_{(J)}):(\tilde{S}_{(J)}-\tilde{\alpha}_{(J)})}}\\
\tilde{\varepsilon}^{p}&={}^{0}\tilde{\varepsilon}^{p}+dp\tilde{n}_{(J)}\\
\tilde{\sigma}&=\tilde{\tilde{C}}:({}^{0}\tilde{\varepsilon}+\Delta\tilde{\varepsilon}-\tilde{\varepsilon}^{p})
\end{aligned}\right\} \tag{A15}$$

Consistent Tangential Model. Once the iteration process described in the last sub-section is convergent, the stress and internal variables are determined. The equilibrium is verified by the global FE equations. If the equilibrium is satisfied, the solution is validated. Otherwise, a new global equilibrium iteration is required. In this case, the consistent tangential matrix $\partial\tilde{\sigma}/\partial\tilde{\varepsilon}|_{\tilde{\alpha},\tilde{\varepsilon}^{p},\tilde{\varepsilon}}$ should be determined to ensure a quadric convergence [47]. This consistent tangential matrix can be obtained from the definition of the deviatoric stress.

Taking the derivatives of Eqs. (*A*9) and (*A*10) with respect to $d\tilde{\varepsilon}$ results in the following equations,

$$-2G\tilde{\tilde{I}}^{\text{dev}}:\delta\tilde{\varepsilon}+\tilde{\tilde{\pi}}:\delta\tilde{\beta}+c_{n}\tilde{n}\,\delta p+\sum_{i=1}^{M}c_{\alpha}^{(i)0}\tilde{\alpha}^{(i)}\delta p=0 \tag{A16}$$

and,

$$\tilde{n}:\delta\tilde{\beta}-\frac{\partial k}{\partial p}\delta p=0 \tag{A17}$$

where $\tilde{\tilde{I}}^{\text{dev}}$ is a fourth order deviatoric tensor that is defined as $\tilde{\tilde{I}}^{\text{dev}}=\tilde{\tilde{I}}-1/3\tilde{1}\otimes\tilde{1}$. $\tilde{\tilde{I}}$ and $\tilde{1}$ present a fourth order and a second order unit tensors, respectively. The symbol $\otimes$ between two tensors denotes the cross product of the tensors. Solving Eqs. (*A*16) and (*A*17), we get,

$$\delta p=\frac{2G\tilde{n}:\tilde{\tilde{\pi}}^{-1}:\tilde{\tilde{I}}^{\text{dev}}:\delta\tilde{\varepsilon}}{D} \tag{A18}$$

and,

$$\delta\tilde{\beta}=\frac{2G}{D}\tilde{\tilde{\pi}}^{-1}:\left(D\tilde{\tilde{I}}-\left(c_{n}\tilde{n}+\sum_{i=1}^{M}c_{\alpha}^{(i)0}\tilde{\alpha}^{(i)}\right)\otimes\tilde{n}:\tilde{\tilde{\pi}}^{-1}\right):\tilde{\tilde{I}}^{\text{dev}}:\delta\tilde{\varepsilon} \tag{A19}$$

Differentiating the evolution equation, Eq. (*A*6), we obtain the expression for the increments of the backstress parts,

$$\delta\tilde{\alpha}^{(i)}=\varsigma^{(i)}\left(\tilde{\tilde{I}}-\frac{c^{(i)}dp\chi^{(i)}(\|\tilde{\alpha}^{(i)}\|/r^{(i)})^{\chi^{(i)}-2}(r^{(i)})^{-2}}{1+(1+\chi^{i})(\|\tilde{\alpha}^{i}\|/r^{i})^{\chi^{i}}c^{i}dp}\tilde{\alpha}^{(i)}\otimes\tilde{\alpha}^{(i)}\right):\left((c^{(i)}r^{(i)}\tilde{n}-c^{(i)}(\|\tilde{\alpha}^{(i)}\|/r^{(i)})^{\chi^{(i)}}\tilde{\alpha}^{(i)})\,\delta p+c^{(i)}r^{(i)}dp\frac{\partial\tilde{n}}{\partial\tilde{\beta}}:\delta\tilde{\beta}\right)\quad(i=1,2,\ldots,M) \tag{A20}$$

The following equation for the stress increment can be derived from the definition of the deviatoric stress,

$$\delta\tilde{\sigma}=\delta\tilde{\beta}+\delta\tilde{\alpha}+K\tilde{1}\otimes\tilde{1}:\delta\tilde{\varepsilon} \tag{A21}$$

where K is the bulk elasticity modulus. Substituting Eqs. (*A*18)–(*A*20) into Eq. (*A*21), a linearized relationship between stress increment and strain increment at time t_{n+1} is obtained.

Appendix B

Illustration of Symbols Used in Eq. (*A*11). The symbols in Eq. (*A*11) are described in the following,

$$\tilde{\tilde{\pi}}=a\left(\tilde{\tilde{I}}+x_{1}\tilde{\gamma}\otimes\tilde{n}-x_{2}\tilde{n}\otimes\tilde{\kappa}-\sum_{i=1}^{M}(\zeta^{(i)}/g)^{0}\tilde{\alpha}^{(i)}\otimes\tilde{\alpha}^{(i)}\right) \tag{B1}$$

$$c_{n}=2G+\sum_{i=1}^{M}c^{(i)}r^{(i)}\left((\varsigma^{(i)})^{2}+\left(r^{(i)}\left(\frac{\|\tilde{\alpha}^{(i)}\|}{r^{(i)}}\right)^{\chi^{(i)}+2}-\tilde{\alpha}^{(i)}:\tilde{n}\right)\zeta^{(i)}\right) \tag{B2}$$

$$c_{\alpha}^{(i)}=\left(\frac{\tilde{\alpha}^{(i)}:\tilde{\alpha}^{(i)}}{r^{(i)}dp}\zeta^{(i)}-(\varsigma^{(i)})^{2}c^{(i)}\right)\left(\frac{\|\tilde{\alpha}^{(i)}\|}{r^{(i)}}\right)^{\chi^{(i)}}-\tilde{\alpha}^{(i)}:\tilde{n}\frac{\zeta^{(i)}}{dp} \tag{B3}$$

where,

$$a=g/\|\beta\| \tag{B4}$$

$$x_{1}=1/g \tag{B5}$$

$$x_{2}=dp/g \tag{B6}$$

$$g=\|\tilde{\beta}\|+\left(2G+\sum_{i=1}^{M}c^{(i)}r^{(i)}\varsigma^{(i)}\right)dp \tag{B7}$$

$$\tilde{\kappa}=\sum_{i=1}^{M}\zeta^{(i)}c^{(i)}r^{(i)}\tilde{\alpha}^{(i)} \tag{B8}$$

$$\tilde{\gamma}=\left(h\tilde{n}+\sum_{i=1}^{M}\zeta^{(i)}(\tilde{\alpha}^{(i)}:\tilde{n})\tilde{\alpha}_{0}^{(i)}\right) \tag{B9}$$

$$h=\sum_{i=1}^{M}\zeta^{(i)}c^{(i)}r^{(i)}dp\tilde{\alpha}^{(i)}:n-\left(2G+\sum_{i=1}^{M}c^{(i)}r^{(i)}\varsigma^{(i)}\right)dp \tag{B10}$$

$$\zeta^{(i)}=\frac{(c^{(i)}\varsigma^{(i)}dp)^{2}\chi^{(i)}/r^{(i)}(\|\tilde{\alpha}^{(i)}\|/r^{(i)})^{\chi^{(i)}-2}}{1+(1+\chi^{(i)})(\|\tilde{\alpha}^{(i)}\|/r^{(i)})^{\chi^{(i)}}c^{(i)}dp} \tag{B11}$$

Appendix C

Lemma. If $\tilde{\gamma}^{i}$ and $\tilde{\kappa}^{j}$ are second-order tensors and the matrix $A=[\Sigma_{k=1}^{m}x_{i}\tilde{\kappa}^{(i)}:\tilde{\gamma}^{(k)}+\delta_{ij}]$ is nonsingular, then the fourth-order tensor $\tilde{\tilde{\pi}}=\tilde{\tilde{I}}+\Sigma_{i=1}^{m}x_{i}\tilde{\gamma}^{(i)}\otimes\tilde{\kappa}^{(i)}$ is invertible and

$$\tilde{\tilde{\pi}}^{-1}=\tilde{\tilde{I}}+\sum_{i,j=1}^{m}y_{ij}\tilde{\gamma}^{(i)}\otimes\tilde{\kappa}^{(j)} \tag{C1}$$

where y_{ij} is the solution of the equation $Ay_{ij} = -x_i\delta_{ij}$, δ_{ij} is the Kronecker delta, and $\tilde{\tilde{I}}$ is the fourth-order unit tensor.

The lemma can be proven by conducting the inner product between $\tilde{\tilde{\pi}}$ and $\tilde{\tilde{\pi}}^{-1}$.

References

[1] Johnson, K. L., 1985, *Contact Mechanics*, Cambridge University Press.

[2] Smith, J. O., and Liu, C. K., 1953, ''Stresses Due to Tangential and Normal Loads on an Elastic Solid with Application to Some Contact Stress Problems,'' ASME J. Appl. Mech., **20**, pp. 157–166.

[3] Sackfield, A., and Hills, D. A., 1983, ''Some Useful Results in the Classical Hertzian Contact Problem,'' J. Strain Anal. Eng. Des., **18**, pp. 101–105.

[4] Sackfield, A., and Hills, D. A., 1983, ''Some Useful Results in the Tangentially Loaded Hertzian Contact Problem,'' J. Strain Anal. Eng. Des., **18**, pp. 107–110.

[5] Merwin, J. E., and Johnson, K. L., 1963, ''An Analysis of Plastic Deformation in Rolling Contact,'' *Proceedings, Institution of Mechanical Engineers, London*, **177**, pp. 676–685.

[6] Bower, A. F., and Johnson, K. L., 1989, ''The Influence of Strain Hardening on Cumulative Plastic Deformation in Rolling and Sliding Line Contact,'' J. Mech. Phys. Solids, **37**, pp. 471–493.

[7] McDowell, D. L., and Moyar, G. J., 1991, ''Effects of Non-Linear Kinematic Hardening on Plastic Deformation and Residual Stresses in Rolling Line Contact,'' Wear, **144**, pp. 19–37.

[8] Jiang, Y., and Sehitoglu, H., 1994, ''An Analytical Approach to Elastic-Plastic Stress Analysis of Rolling Contact,'' ASME J. Tribol., **116**, pp. 577–587.

[9] Jiang, Y., and Sehitoglu, H., 1996, ''Rolling Contact Stress Analysis with the Application of a New Plasticity Model,'' Wear, **191**, pp. 35–44.

[10] Xu, B., and Jiang, Y., 2002, ''Elastic-Plastic Finite Element Analysis of Partial Slip Rolling Contact,'' ASME J. Tribol., **124**, pp. 20–26.

[11] Bhargava, V., Hahn, G. T., and Rubin, C. A., 1983, ''An Elastic-Plastic Finite Element Model of Rolling Contact. Part I: Single Contacts; Part II: Repeated Contacts,'' ASME J. Appl. Mech., **52**, pp. 66–82.

[12] Hahn, G. T., and Huang, Q., 1986, ''Rolling Contact Deformation of 1100 Aluminum Disks,'' Metall. Trans. A, **17**, pp. 1561–1571.

[13] Hahn, G. T., Bhargava, V., Rubin, C. A., Chen, Q., and Kim, K., 1987, ''Analysis of the Rolling Contact Residual Stresses and Cyclic Plastic Deformation of SAE52100 Steel Ball Bearings,'' ASME J. Tribol., **109**, pp. 618–626.

[14] Kumar, A. M., Hahn, G. T., Bhargava, V., and Rubin, C. A., 1989, ''Elasto-Plastic Finite Element Analyses of Two-Dimensional Rolling and Sliding Contact Deformation of Bearing Steel,'' ASME J. Tribol., **111**, pp. 309–314.

[15] Bhargava, V., Hahn, G. T., Ham, G., Kulkarni, S., and Rubin, C. A., 1990, ''Influence of Kinematic Hardening on Rolling Contact Deformation,'' *Proceedings of the Third International Symposium on Contact Mechanics and Wear of Rail/Wheel Systems*, Cambridge, U.K., pp. 133–146.

[16] Howell, M., Hahn, G. T., Rubin, C. A., and McDowell, D. L., 1995, ''Finite Element Analysis of Rolling Contact for Non-Linear Kinematic Hardening Bearing Steel,'' ASME J. Tribol., **117**, pp. 729–736.

[17] Jiang, Y., Chang, J., and Xu, B., 2001, ''Elastic-Plastic Finite Element Stress Analysis of Two-dimensional Rolling Contact,'' *Hydraulic Failure Analysis: Fluids, Components, and System Effects*, ASTM STP 1339, Totten, Wills, and Feldmann, eds., American Society for Testing and Materials, West Conshohocken, PA, pp. 59–74.

[18] Dan Van, K., and Maitournam, M. H., 1993, ''Steady-State Flow in Classical Elastoplasticity: Applications to Repeated Rolling and Sliding Contact,'' J. Mech. Phys. Solids, **41**, pp. 1691–1710.

[19] Ham, G. L., Hahn, G. T., Rubin, C. A., and Bhargava, V., 1989, ''Finite Element Analysis of the Influence of Kinematic Hardening in Two-Dimensional, Repeated, Rolling-Sliding Contact,'' Tribol. Trans., **32**, pp. 311–316.

[20] Hamilton, G. M., 1963, ''Plastic Flow in Rollers Loaded above the Yield Point,'' *Proceedings, Institution of Mechanical Engineers*, London, **177**, pp. 667–675.

[21] Shima, M., Okada, K., Kimura, Y., and Yamamoto, T., 1981, ''Measurements of Subsurface Plastic Flow in Rolling Contact,'' Journal of JSLE, International Edition, **2**, pp. 75–80.

[22] Kulkarni, S., Hahn, G. T., Rubin, C. A., and Bhargarva, V., 1990, ''Elastoplastic Finite Element Analysis of Three-Dimensional Pure Rolling Contact at the Shakedown Limit,'' ASME J. Appl. Mech., **57**, pp. 57–65.

[23] Kulkarni, S., Hahn, G. T., Rubin, C. A., and Bhargarva, V., 1990, ''Elastoplastic Finite Element Analysis of Three-Dimensional Pure Rolling Contact Above the Shakedown Limit,'' ASME J. Appl. Mech., **58**, pp. 347–353.

[24] Kulkarni, S., Hahn, G. T., Rubin, C. A., and Bhargarva, V., 1991, ''Elasto-Plastic Finite Element Analysis of Repeated Three-dimensional, Elliptical Rolling Contact with Rail Wheel Properties,'' ASME J. Tribol., **113**, pp. 434–441.

[25] Jiang, Y., and Kurath, P., 1996, ''Characteristics of the Armstrong-Frederick Type Plasticity Models,'' Int. J. Plast., **12**, pp. 387–415.

[26] Jiang, Y., and Kurath, P., 1997, ''An Investigation of Cyclic Transient Behavior and Implications on Fatigue Life Estimates,'' ASME J. Eng. Mater. Technol., **119**, pp. 161–170.

[27] Jiang, Y., and Sehitoglu, H., 1994, ''Cyclic Ratchetting of 1070 Steel under Multiaxial Stress State,'' Int. J. Plast., **10**, pp. 579–680.

[28] Jiang, Y., and Sehitoglu, H., 1994, ''Multiaxial Cyclic Ratchetting Under Multiple Step Loading,'' Int. J. Plast., **10**, pp. 849–870.

[29] Bower, A. F., and Johnson, K. L., 1990, ''Plastic Flow and Shakedown of the Rail Surface in Repeated Wheel-Rail Contact,'' *Third International Symposium on Contact Mechanics and Wear of Rail/Wheel Systems*, Cambridge, UK.

[30] Johnson, K. L., 1990, ''A Graphical Approach to Shakedown in Rolling Contact,'' in *Applied Stress Analysis*, Hyde and Ollerton, eds., Elsevier Applied Science, pp. 263–274.

[31] Ponter, A. R. S., 1976, ''A General Shakedown Theorem for Elastic-Plastic Bodies With Work Hardening,'' *The Third International Conference on Structural Mechanics in Reactor Technology*, London.

[32] Jiang, Y., and Kurath, P., 1997, ''Nonproportional Cyclic Deformation: Critical Experiments and Analytical Modeling,'' Int. J. Plast., **13**, pp. 743–763.

[33] Chaboche, J. L., Dang Dan, K., and Cordier, G., 1979, ''Modelization of the Strain Memory Effect on the Cyclic Hardening of 316 Stainless Steel,'' *Transactions of the Fifth International Conference on Structural Mechanics in Reactor Technology*, Div. L, Berlin, L11/3.

[34] Chaboche, L. J., 1987, ''Cyclic Plasticity Modeling and Ratchetting effects,'' *Proceedings of the 2nd International Conference on Constitutive Laws for Engineering Materials: Theory & Application*, Tucson, Arizona, Desal et al., Eds., Elsevier, pp. 47–58.

[35] Chaboche, L. J., 1991, ''On Some Modifications of Kinematic Hardening to Improve the Description of Ratcheting Effects,'' Int. J. Plast., **7**, pp. 661–687.

[36] Armstrong, P. J., and Frederick, C. O., 1966, ''A Mathematical Representation of the Multiaxial Bauschinger Effect,'' Report RD/B/N 731, Central Electricity Generating Board.

[37] Ohno, N., and Wang, J. D., 1991, ''Nonlinear Kinematic Hardening Rule: Proposition and Application to Ratchetting Problems,'' 11th SMiRT, Shibata, ed., Vol. L, Tokyo, Japan, L22/1, pp. 481–486.

[38] Ohno, N., and Wang, J. D., 1991, ''Nonlinear Kinematic Hardening Rule With Critical State for Activation of Dynamic Recovery,'' PLASTICITY'91, Boehler and Khan, eds., Grenoble, France, pp. 455–458.

[39] Ohno, N., and Wang, J. D., 1993, ''Kinematic Hardening Rules with Critical State of Dynamic Recovery: Part I—Formulation and Basic Features for Ratchetting Behavior,'' Int. J. Plast., **9**, pp. 375–390.

[40] Ohno, N., and Wang, J. D., 1993, ''Kinematic Hardening Rules with Critical State of Dynamic Recovery: Part II: Application to Experiments of Ratchetting Behavior,'' Int. J. Plast., **9**, pp. 391–403.

[41] Jiang, Y., and Sehitoglu, H., 1996, ''Modeling of Cyclic Ratchetting Plasticity: Part I—Development of Constitutive Equations,'' ASME J. Appl. Mech., **63**, pp. 720–725.

[42] Jiang, Y., and Sehitoglu, H., 1996, ''Modeling of Cyclic Ratchetting Plasticity: Part II—Implement of the New Model and Comparison of Theory with Experiments,'' ASME J. Appl. Mech., **63**, pp. 726–733.

[43] Ohno, N., and Wang, J. D., 1994, ''Kinematic Hardening Rules for Simulation of Ratchetting Behavior,'' Eur. J. Mech. A/Solids, **13**, pp. 519–531.

[44] Jiang, Y., and Kurath, P., 1996, ''A Theoretical Evaluation of The Incremental Plasticity Hardening Algorithms for Cyclic Nonproportional Loadings,'' Acta Mech., **118**, pp. 213–234.

[45] Jiang, Y., and Sehitoglu, H., 1999, ''A Model for Rolling Contact Failure,'' Wear, **224**, pp. 38–49.

[46] *ABAQUS/Standard User's Manual*, 1999, Hibbitt, Karlsson and Sorensen, Inc.

[47] Simo, J., and Taylor, R. L., 1985, ''Consistent Tangent Operators for Rate-Independent Elastoplasticity,'' Comput. Methods Appl. Mech. Eng., **48**, pp. 101–118.